RSC Advances

PAPER

View Article Online
View Journal | View Issue

Open Access Article. Published on 02 January 2024. Downloaded on 1/16/2026 5:07:56 PM.
This article is licensed under a Creative Commons Attribution-NonCommercial 3.0 Unported Licence.

Cite this: *RSC Adv.*, 2024, **14**, 118

Construction of a uniform zeolitic imidazole framework (ZIF-8) nanocrystal through a wet chemical route towards supercapacitor application†

Iqra Rabani,*[a] Je-Won Lee,[a] Taeyoon Lim,[a] Hai Bang Truong,[bc] Sobia Nisar,[d] Sitara Afzal[e] and Young-Soo Seo *[a]

Received 12th October 2023
Accepted 5th November 2023

DOI: 10.1039/d3ra06941a

rsc.li/rsc-advances

Exploring larger surface area electrode materials is crucial for the development of an efficient supercapacitors (SCs) with superior electrochemical performance. Herein, a cost-effective strategy was adopted to synthesize a series of ZIF8 nanocrystals, and their size effect as a function of surface area was also examined. The resultant ZIF8-4 nanocrystal exhibits a uniform hexagonal structure with a large surface area (2800 m^2 g^{-1}) and nanometre size while maintaining a yield as high as 78%. The SCs performance was explored by employing different aqueous electrolytes (0.5 M H_2SO_4 and 1 M KOH) in a three-electrode set-up. The SC performance using a basic electrolyte (1 M KOH) was superior owing to the high ionic mobility of K^+. The optimized ZIF8-4 nanocrystal electrode showed a faradaic reaction with a highest capacitance of 1420 F g^{-1} at 1 A g^{-1} of current density compared to other as-prepared electrodes in the three-electrode assembly. In addition, the resultant ZIF8-4 was embedded into a symmetric supercapacitor (SSC), and the device offered 350 F g^{-1} of capacitance with a maximum energy and power density of 43.7 W h kg^{-1} and 900 W kg^{-1} at 1 A g^{-1} of current density, respectively. To determine the practical viewpoint and real-world applications of the ZIF8-4 SSC device, 7000 GCD cycles were performed at 10 A g^{-1} of current density. Significantly, the device exhibited a cycling stability around 90% compared to the initial capacitance. Therefore, these findings provide a pathway for constructing large surface area ZIF8-based electrodes for high-value-added energy storage applications, particularly supercapacitors.

1. Introduction

Tremendous attempts have been made by the scientific community to store and convert energy to meet the needs of renewable and uninterrupted energy and power sources for portable electronics, power-supply devices and powering vehicles.[1,2] To date, the most concerning energy resource is electrical energy following fossil fuels, which has become the necessity of life for applications ranging from lighting to communication.[3] Batteries and supercapacitors are considered the two most prevalent types of electrochemical energy storage devices.[4] Depending on the output power delivery, no other electrochemical energy storage device can compete with supercapacitors.[5,6] Supercapacitors are classified into two types depending on the charge storage mechanism: redox capacitors, in which faradaic reactions are responsible for the capacitance, and electric double layer capacitors (EDLCs), wherein the charge separation mechanism occurring at the interface of the electrode–electrolyte is accountable for the capacitance.[7–9]

To improve the supercapacitor performance, a breakthrough in electrode materials is a substantial factor. Up to now, the most explored electrodes of EDLCs are advanced carbon materials owing to their exceptional benefits, such as an outstanding electrical conductivity, extraordinary chemical stability, cost-effectiveness, enlarged surface area, and tailored pore structures.[10,11] As precursors, metal–organic frameworks (MOFs) and covalent organic materials (COMs) are desirable owing to their enriched surface areas, structural diversity and pore controlling characteristics.[12–14] Highly nano-porous carbon materials are obtained from MOFs and COMs, which are excessively utilized

---

[a] *Department of Nanotechnology and Advanced Materials Engineering, Sejong University, Seoul 05006, Republic of Korea. E-mail: iqrarabani@sejong.ac.kr; ysseo@sejong.ac.kr*

[b] *Optical Materials Research Group, Science and Technology Advanced Institute, Van Lang University, Ho Chi Minh City, Viet Nam. E-mail: truonghaibang@vlu.edu.vn*

[c] *Faculty of Applied Technology, School of Engineering and Technology, Van Lang University, Ho Chi Minh City, Viet Nam*

[d] *Department of Electronic Engineering, Sejong University, Seoul 05006, Republic of Korea*

[e] *Mixed Reality and Interaction Laboratory, Sejong University, Seoul 05006, Republic of Korea*

† Electronic supplementary information (ESI) available. See DOI: https://doi.org/10.1039/d3ra06941a

© 2024 The Author(s). Published by the Royal Society of Chemistry

Open Access Article. Published on 02 January 2024. Downloaded on 1/16/2026 5:07:56 PM. This article is licensed under a Creative Commons Attribution-NonCommercial 3.0 Unported Licence.

for clean energy applications, such as an ORR in fuel cells, sensing, gas adsorption, pollution treatment and supercapacitors.[1,15–20] The reported capacitances of the carbon supercapacitor electrodes are far less than those of the MOF-derived carbon materials because of their micropore diameters and high surface areas.[21] The design of super capacitive electrodes remains a challenge to meet the requirements of high energy density, excellent capacitance, and outstanding stability.[22]

To this end, MOFs are the most desired class of crystalline porous materials and are not only an attractive precursor but also the best template for the fabrication of carbon-based porous materials.[23,24] The zeolitic imidazolate framework (ZIF) is a subset of MOFs. The network of ZIF is designed by the interlinking of metal ions with imidazolate anions whose strong interaction bestows a highly robust rigid-cage-like structure.[25,26] The most crucial components of ZIFs, *i.e.*, metal ions and imidazole ligands, significantly impact the pore and topological structure of ZIFs by changing their types. Different ZIFs possess the same topological structures, and ZIFs with similar metal ions and imidazole ligands possess distinct topological structures.[27,28] Among the ZIFs, ZIF-8 is one of the considerable compositions owing to its low cost, high chemical and thermal stability, easy synthesis process, high nitrogen content, high porosity and larger surface area.[29,30] Based on the previous literature, nitrogen atoms can significantly improve the capacitance because of the pseudocapacitance contribution, and the nitrogen content can improve the wettability of the carbon interface in aqueous electrolytes and enhance their contact.[31–34]

However, the use of ZIF-8 nanocrystals in supercapacitor applications faces two main challenges: (1) their intrinsic low conductivity of ZIF-based material hinders the charge transfer in the framework and therefore significantly restricts their overall electrochemical consequences and (2) the larger crystal size averts the electrolyte from contacting deep pores and outcomes in the inadequate utilization of the surface, reducing the overall capacitance.[35] Therefore, there is a critical requirement to construct reasonable approaches for controllable synthesis with high electric conductivity and a highly accessible surface area.

In this work, a series of ZIF8 nanocrystals was demonstrated through a one-step wet chemical route (Scheme 1). Significantly, the surface area was improved by decreasing the size of the ZIF8 crystal and then probing supercapacitor performance using different electrolytes, including acidic (0.5 M H_2SO_4) and basic (1 M KOH), in a three-electrode assembly in detail. Significantly, SC performance using a basic electrolyte (1 M KOH) was superior owing to the higher ionic mobility of K^+. Among all, the ZIF8-4 nanocrystals exhibit the faradaic reaction with the highest capacitance of 1420 F g^{-1} using 1 M KOH in a three-electrode assembly at 1 A g^{-1} of current density compared with the ZIF8-1 (344.2 F g^{-1}), ZIF8-2 (545 F g^{-1}) and ZIF8-3 (693.3 F g^{-1}) nanocrystal electrodes. Further, a symmetric supercapacitor (SC) was fabricated using optimized ZIF8-3 and ZIF8-4 nanocrystal electrodes. As expected, the ZIF8-4 SSC device exhibited the highest capacity (350 F g^{-1}), maximum energy and power density (43.7 W h kg^{-1}, 900 W kg^{-1}) at 1 A g^{-1} of current density, and superior cycling stability (90% over 7000 cycles) at 10 A g^{-1} of current density.

2. Materials and methods

2.1 Materials

The zinc nitrate hexahydrate ($Zn(NO_3)_2\cdot 6H_2O$), 2-methylimidazole (2-MIM), carbon black, polyvinyl dene fluoride (PVDF), *N*-methylene propylene (NMP), methanol (MeOH) and ethanol (EtOH) were bought from Sigma-Aldrich, South Korea. All the chemicals were purchased from the suppliers directly. The nickel plate (Ni) as a current collector and nickel foam (NF, 1.6 mm thickness) as a substrate for the working electrode, obtained from ALANTUM, South Korea, were carefully cleaned with ethanol, acetone, and deionized (DI) water.

2.2 Synthesis of ZIF8 crystals

The wet chemical method was employed to prepare ZIF8 with controlled morphology by changing the concentration of the precursors and reaction time, and the samples were labelled ZIF8-1, ZIF8-2, ZIF8-3, and ZIF8-4. Scheme 1 presents the synthesis process of the ZIF8 nanocrystals. In this process, Zn salt was dissolved in MeOH, and 2-methylimidazole (2-MIM) was added to MeOH under different ratios. The organic linker (2-MIM; 800 mg) was then abruptly poured into the inorganic solution (Zn salt; 800 mg) at a continuous stirring speed of 300 rpm for about 2 h. The obtained white precipitates were cleansed several times with MeOH; then, the final product was dried in a vacuum oven overnight at 75 °C. The final product was labelled by the ZIF8-4 nanocrystals, and other ZIF8 nanocrystals were also synthesized similarly except for the precursor concentration at constant reaction time (Table 1).

2.3 Material characterizations

The morphology and structural analysis of the as-prepared samples were investigated through field-emission scanning

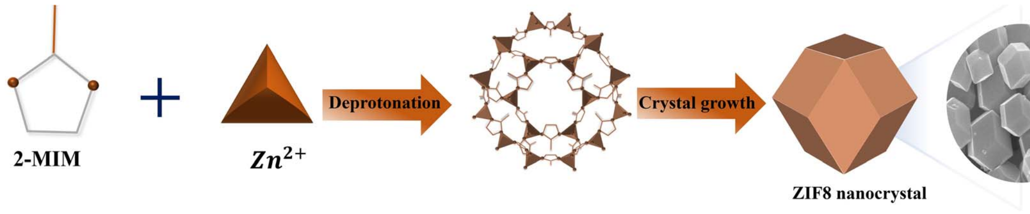

Scheme 1 An illustration of the synthesis of the ZIF8 nanocrystals.

Table 1 Experimental conditions and crystal size variations of synthesized ZIF8

Experiments	Sample	Zn $(NO_3)_2 \cdot 6H_2O$: 2-MIM	Crystal size (nm)	Reaction time (h)
1	ZIF8-1	2 : 1	250	3
2	ZIF8-2	1.5 : 1	896	3
3	ZIF8-3	1 : 1	660	3
4	**ZIF8-4**	**1 : 1**	100	2

Open Access Article. Published on 02 January 2024. Downloaded on 1/16/2026 5:07:56 PM. This article is licensed under a Creative Commons Attribution-NonCommercial 3.0 Unported Licence.

electron microscopy (FE-SEM; Hitachi, SU-8010, 5.0 kV, working distance: 6.8 mm) and high-resolution transmission electron microscopy (TEM; JEM-2010, 200 kV). Chemical composition analysis was performed using the energy dispersive X-ray (EDX) technique operating at 5 kV and 10 keV. X-ray diffraction spectroscopy (PANalytical XRD-6100 instrument with Cu Kα radiation ($\lambda = 1.5406$ Å) at a scan speed of 5° min^{-1}) was used for the investigation of the crystal structure in the 2θ range of 10–50°. A confocal Raman microscope was employed to conduct the Raman spectra with a signal wavelength of 632 nm (He–Ne source) using a Raman spectrometer (JASCO, NRS-3100) under ambient conditions. The surface characteristics of the as-prepared samples were studied using nitrogen (N_2) adsorption/desorption isotherms (BET, Micromeritics-ASAP-2020).

2.4 Electrochemical measurement

The electrochemical analysis was performed in a conventional three-electrode assembly in an aqueous 1.0 M KOH electrolyte. A platinum wire and Hg/HgO were employed as counter and reference electrodes, respectively. The working electrode was prepared by employing an active material on the substrate. The nickel foam was used as a substrate, and the as-synthesized materials (ZIF8-1, ZIF8-2, ZIF8-3 and ZIF8-4 nanocrystal electrodes) acted as active material. Briefly, the 80 : 10 : 10 ratio of the active material, carbon black and polyvinyl dene fluoride (PVDF) were added into the mortar and then ground using the NMP solvent to obtain the uniform slurry. The slurry was pasted on the Ni foam and then dried in a vacuum oven (100 °C and 12 h). Cyclic voltammetry (CV) and galvanostatic charging–discharging (GCD) profiles were performed using the Biologic SP 150 workstation. The electrochemical impedance spectroscopy (EIS) measurements were recorded at the frequency range of 100 kHz–0.01 Hz with an AC amplitude of 5 mV under the open circuit voltage. The specific capacitance (C_s) was calculated using the following equation:[34]

$$C_s = \frac{I \times \Delta t}{m \times \Delta V}, \tag{1}$$

where I is the current in mA, Δt is the discharging time in seconds, m is the loading mass in mg, and ΔV is the voltage window at the volts.

2.5 Assembly of the symmetric supercapacitor

A symmetric supercapacitor was assembled by sandwiching a piece of wet separator (the PVDF membrane was immersed in 1.0 M KOH) between two identical as-synthesized electrodes (optimized ZIF8-3 and ZIF8-4 nanocrystal electrodes) and placed between the parafilm. Afterwards, constant pressure (100 kPa) was applied on top of the parafilm to ensure stable electrical contact between the electrodes and electrolytes. A symmetric supercapacitor was obtained for further measurement of the electrochemical parameters. The C, energy density (E) and power density (P) were determined based on the GCD profile by applying the following equation:[36]

$$C_s = \frac{2 \times I \times \Delta t}{m \times \Delta V}, \tag{2}$$

$$E = \frac{C_s \times \Delta v^2}{8}, \tag{3}$$

$$P = \frac{3.6 \times E}{\Delta t}, \tag{4}$$

where I, Δt, m, ΔV, E and P are the current in mA, discharging time in sec, loading mass in mg, voltage window in volts, energy density in W h kg^{-1} and power density in kW kg^{-1}.

3. Results and discussions

3.1 Materials characterizations

The wet-chemical route-based synthesis formation of ZIF8 nanocrystals is illustrated in Scheme 1. To optimize the crystal size effect for the EES purpose, the inorganic and organic concentrations and reaction time were varied. The surface topographies for the series of the ZIF8 nanocrystals under different synthesis conditions were characterized using FESEM analysis, and the corresponding images are shown in Fig. 1(a)–(h). As shown in Fig. 1(a) and (b), the ZIF8-1 (Zn : 2-MIM :: 2 : 1, 3 h) shows a rough-like surface morphology with a hexagonal structure, and about 80% yield was obtained. The crystal size was found to be approximately 250 nm. When the concentration of the inorganic precursors was low (Zn : 2-MIM :: 1.5 : 1) at the same reaction time, the crystal size of ZIF8-2 increased three times with the visible hexagonal structure, as depicted in Fig. 1(c) and (d). The productivity loss through synthesis was only 2%. In the next study, the ZIF8-3 exhibits a uniform hexagonal structure with the same reaction time at the same inorganic and organic precursor concentrations (Zn : 2-MIM :: 1 : 1); the corresponding images are depicted in Fig. 1(e) and (f). The crystal size decreased by 1.3% for ZIF8-2 and expanded by 2.5% for ZIF8-1 with a satisfactory yield from ZIF8-3 nanocrystals (75%). Unfortunately, the synthesized

© 2024 The Author(s). Published by the Royal Society of Chemistry

Open Access Article. Published on 02 January 2024. Downloaded on 1/16/2026 5:07:56 PM.
This article is licensed under a Creative Commons Attribution-NonCommercial 3.0 Unported Licence.

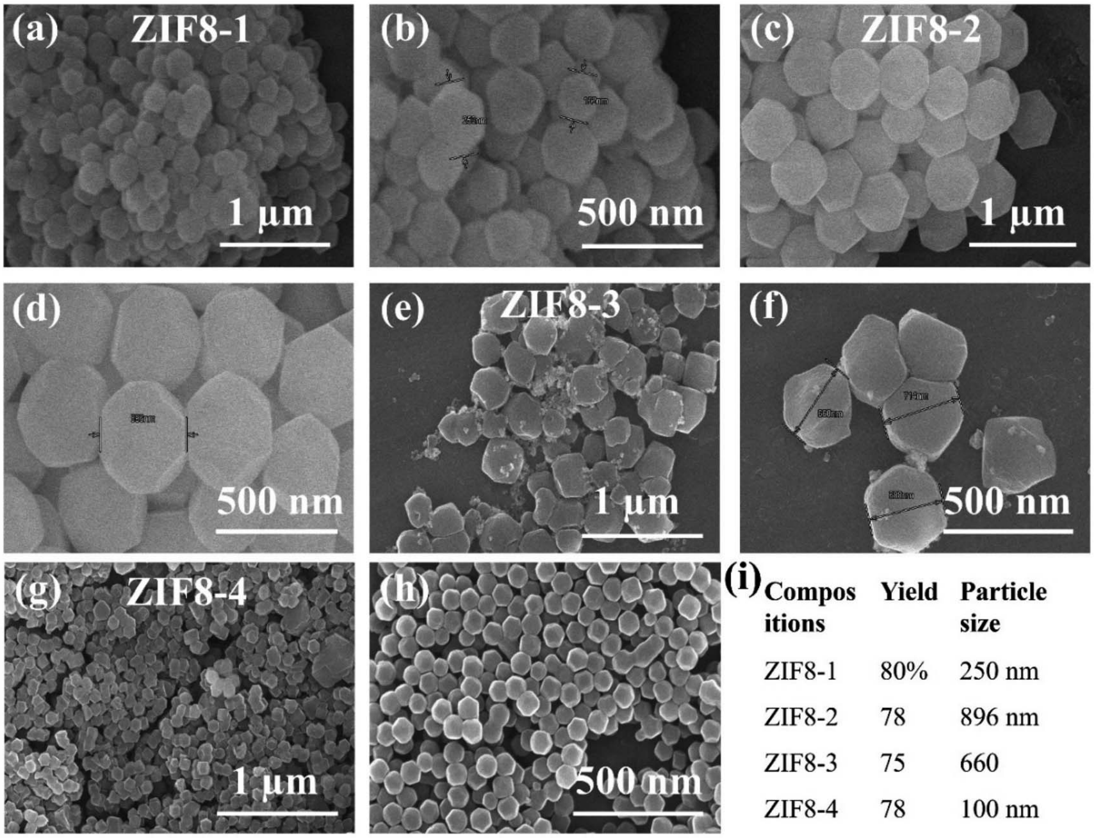

Compositions	Yield	Particle size
ZIF8-1	80%	250 nm
ZIF8-2	78	896 nm
ZIF8-3	75	660
ZIF8-4	78	100 nm

Fig. 1 FESEM micrographs of the series of ZIF8 nanocrystals: (a and b) ZIF8-1 (Zn : 2-MIM :: 2 : 1, 3 h), (c and d) ZIF8-2 (Zn : 2-MIM :: 1.5 : 1, 3 h), (e and f) ZIF8-3 (Zn : 2-MIM :: 1 : 1, 3 h), (g and h) ZIF8-4 (Zn : 2-MIM :: 2 : 1, 2 h), and (i) summary of ZIF8 nanocrystals as a function of the yield and particle size.

products did not meet the requirements for improving the EES application. To meet the need for EES, we further optimized the smaller crystal size while maintaining the yield, thus increasing the surface area. As depicted in Fig. 1(g) and (h), the images of ZIF8-4 were obtained for 2 h with the same concentration of ZIF8-3, which shows a further cutback in crystal size to approximately 100 nm, while increasing the yield by 3%. Conspicuously, the ZIF8-4 crystals retained a well-defined hexagonal morphology with high crystallinity despite their smaller size. Generally, the reduction in crystal size is credited to the high nucleation rate of ZIF8 crystals in the beginning during the synthesis reaction, resulting in the formation of numerous small crystals that combine to form a larger crystal as the reaction progresses.[37] Reducing the reaction time by modifying the concentration, no well-defined structure was found when the reaction was performed. Therefore, no further testing was performed for the synthesis. A summary of all the conducted experiments is presented in Table 1 in detail (Fig. 1i).

To probe the FESEM findings, TEM analysis was performed on the optimized ZIF8-4 nanocrystal, as shown in Fig. 2(a)–(d), at low and high magnifications. The obtained results showed that ZIF8-4 nanocrystals had a hexagonal shape without the deterioration of sodalite morphology while reducing the reaction time from 3 h to 2 h with a fixed concentration (Zn : 2-MIM :: 1 : 1), as shown in Fig. 2(a) and (b). In a magnified view of the ZIF8-4 nanocrystals at 10 nm magnifications, smooth and uniform hexagonal edges were observed with high crystallinity; the micrographs are presented in Fig. 2(c) and (d). To further confirm the presence of the elemental mapping analysis, the EDX study was performed, and the resulting images are shown in Fig. 2(e)–(i). It is obvious from the EDX analysis that the ZIF8-4 nanocrystals are primarily composed of C (blue), O (green), N (red) and Zn (yellow), as depicted in Fig. 2(e)–(h). The selected area of the elemental mapping with the atomic percentage of the elements is depicted in Fig. 2(i) and inset one, where the atomic percentages of C, O, N and Zn are 52.03%, 3.02%, 19.85% and 25.1%, respectively. All the above characterizations support the successful synthesis formation of ZIF8-4 nanocrystals.

The crystallinity and phase compositions of the as-prepared series of ZIF8-1, ZIF8-2, ZIF8-3 and ZIF8-4 nanocrystals were investigated by performing XRD analysis, and the obtained diffractograms are shown in Fig. 3(a). In the case of all as-prepared ZIF8 nanocrystals, the sharp and prominent reflection peaks situated at $2\theta = 7.21°$ and $12.81°$ correspond to the crystal planes of (011) and (112)[38,39] for the series of ZIF8 nanocrystals. The presence of other characteristics, such as (002), (022), (013) and (222) at the $2\theta = 10.3°$, $14.7°$, $16.3°$ and $17.9°$, respectively, confirms the correct formation of ZIF8-based nanocrystals. Therefore, these observations are well-matched with the standard diffraction patterns with JCPDS card no. 00-062-1030.[38,40] However, a low width with a sharp

Open Access Article. Published on 02 January 2024. Downloaded on 1/16/2026 5:07:56 PM.
This article is licensed under a Creative Commons Attribution-NonCommercial 3.0 Unported Licence.

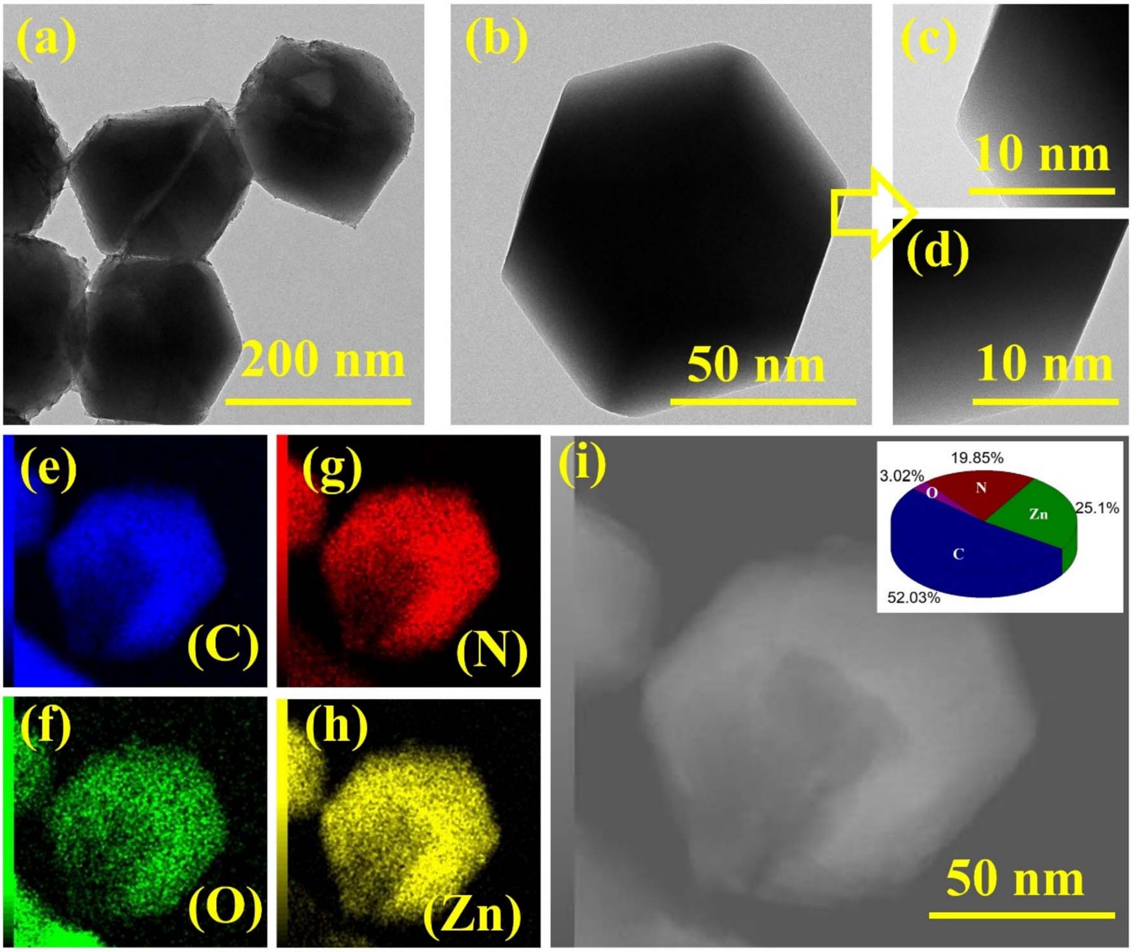

Fig. 2 TEM micrographs of the optimized ZIF8-4 nanocrystals: (a–d) ZIF8-4 (Zn : 2-MIM :: 1 : 1, 2 h) and (e–i) EDS mapping with the elements of (e) C (blue), (f) O (green), (g) N (red), (h) Zn (yellow) and (i) selected area of EDS mapping with atomic% of elements in the inset.

peak was observed in the ZIF8-4 nanocrystals owing to the reduced crystal size with uniform morphology, suggesting a reduction in the crystallinity of ZIF8 nanocrystals. In contrast, the synthesized ZIF8-1 nanocrystals showed a disturbing pattern for clear visibility, as shown in Fig. S1.† The ZIF8 crystalizes in a cubic crystal system with a topology of $I\bar{4}3m$ space group symmetry, as depicted in the inset in Fig. 3(a).

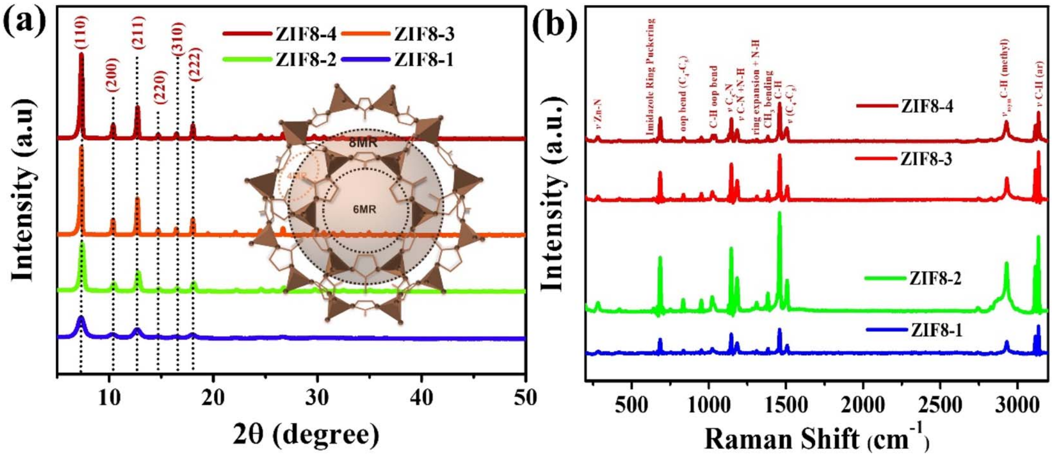

Fig. 3 (a) XRD patterns of the ZIF8-1, ZIF8-2, ZIF8-3 and ZIF8-4 nanocrystals and (b) Raman analysis for the ZIF8-1, ZIF8-2, ZIF8-3 and ZIF8-4 nanocrystals.

© 2024 The Author(s). Published by the Royal Society of Chemistry

Open Access Article. Published on 02 January 2024. Downloaded on 1/16/2026 5:07:56 PM. This article is licensed under a Creative Commons Attribution-NonCommercial 3.0 Unported Licence.

In addition to analyzing the surface chemistry of the prepared series of ZIF8 nanocrystals, a laser Raman spectroscopy study was conducted under ambient conditions, and the results are demonstrated in Fig. 3(b). As depicted in Fig. 3(b), the high-resolution Raman analysis showed numerous peaks under an incident laser of 633 nm, resulting in the stretching, bending, aromatic, out-of-plane and asymmetric bonds for the ZIF8-1, ZIF8-2, ZIF8-3 and ZIF8-4 nanocrystals, respectively.[41] Specifically, the band detected at 282 cm^{-1} corresponds to Zn–N stretching, while the bands monitored at 686 cm^{-1} were attributed to the imidazolium ring puckering, and 1146 cm^{-1} and 1460 cm^{-1} described the C5–N stretching and methyl bending, respectively. Significantly, the methyl group originated from the antisymmetric stretching band in C–H at 2930 cm^{-1}.[39,42] In addition, the vibrational band around 1313 cm^{-1} corresponds to the C–H stretching bands of the imidazole ring. Therefore, a slight shift in the peaks was associated with the various crystal sizes of ZIF8.[39,42] The availability of all these vibrational bands validates the successful synthesis formation of ZIF8 nanocrystals. In particular, the band assignments in a detailed manner have been specified in Table S1† according to the state-of-art-literature.[41,43]

To understand the porous nature, including the specific surface area, pore volume and pore diameter of the as-prepared series of ZIF8 nanocrystals, BET measurements at 77 K of temperature in liquid nitrogen were conducted. The resultant isotherm profiles are shown in Fig. 4(a). Based on the IUPAC classifications, the ZIF8-1, ZIF8-2, ZIF8-3 and ZIF8-4 nanocrystals show the type-IV adsorption with the hysteresis loop H3 because of the capillary condensation, demonstrating the mesoporous nature,[44] and the results are illustrated in Fig. 4(a). The ZIF8-4 nanocrystals had the highest surface area of 2800 $m^2\ g^{-1}$ compared with the other ZIF8-3 (2100 $m^2\ g^{-1}$), ZIF8-2 (1138 $m^2\ g^{-1}$), and ZIF8-1 (1066 $m^2\ g^{-1}$). The pore size distributions and cumulative pore volume were probed using BJH assessments, and the average pore volumes were 0.231, 0.691, 1.73 and 2.41 $cm^3\ g^{-1}$, for the ZIF8-1, ZIF8-2, ZIF8-3 and ZIF8-4 nanocrystals, respectively. Thus, the high crystallinity and uniform hexagonal morphology of the ZIF8-4 nanocrystals resulted in the improvement of the surface properties, leading to the creation of open paths for the extraction of electrolyte ions and diffusion during electrochemical measurements.[45]

3.2 Electrochemical analysis (three-electrode assembly)

The electrochemical performance was explored by employing acid (0.5 M H_2SO_4) and basic electrolytes (1 M KOH) to study the difference in specific capacitance as a function of the electrolytes. It is well accepted that the electrolyte is an essential constitute for energy storage applications and contributes a significant role in the haulage of charge. A series of ZIF8 nanocrystals were used as working electrodes, and their overall electrochemical performance was examined in a three-electrode assembly in the applied potential window, ranging from 0.1 to 0.6 V. Initial cyclic voltammetry (CV) and galvanostatic charging–discharging (GCD) tests were conducted to analyze the electrochemical response of the prepared three-electrode set-up. Fig. S2(a)–(d)† illustrates the CV profiles of the ZIF8-1, ZIF8-2, ZIF8-3 and ZIF8-4 nanocrystal electrodes for various scan rates, including 10, 20, 30, 40, 50, 60, 70, 80, 90 and 100 mV s^{-1} using 0.5 M H_2SO_4 aqueous electrolytes. GCD tests were also conducted for all as-fabricated electrodes using 0.5 M H_2SO_4 aqueous electrolytes at different current densities, and the detailed results are shown in Fig. S3(a)–(d).†

The obtained CV and GCD results showed oxidation and reduction shouter peaks during the charging and discharging processes for all the as-fabricated electrodes, which is credited to the pseudocapacitance behaviour. In the case of the ZIF8-4 nanocrystal electrode, the integrated area of CV and the value of current reached a maximum at a scan rate of 10 mV s^{-1} compared to the other as-fabricated electrodes, as shown in Fig. S4(a).† As presented in Fig. S4(b),† the ZIF8-4 nanocrystal electrode shows consistent performance with CV profiles, with the longest discharging distance covered compared to the other electrodes. Significantly, the ZIF8-4 nanocrystal electrode

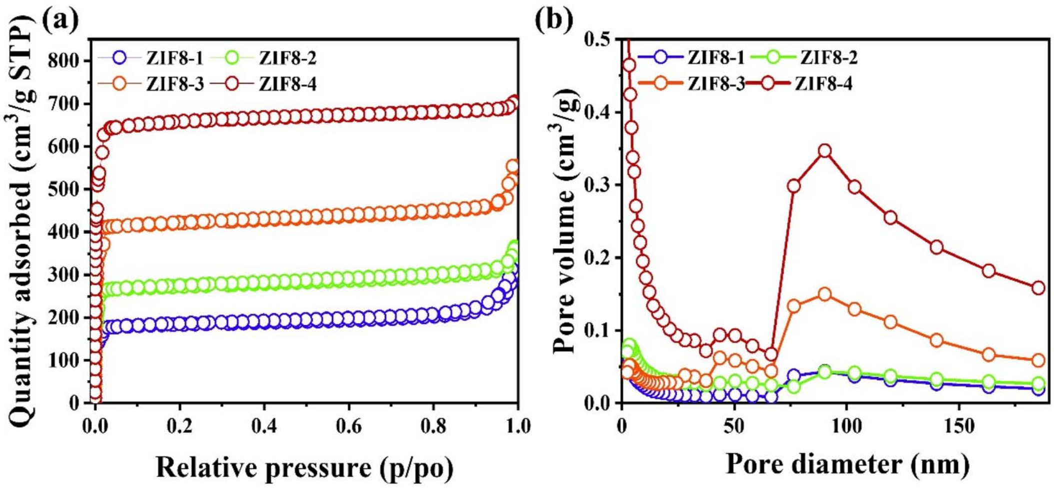

Fig. 4 (a) Adsorption–desorption isotherm plots of ZIF8-1, ZIF8-2, ZIF8-3 and ZIF8-4 nanocrystals and (b) BJH analysis for ZIF8-1, ZIF8-2, ZIF8-3 and ZIF8-4 nanocrystals.

Open Access Article. Published on 02 January 2024. Downloaded on 1/16/2026 5:07:56 PM.
This article is licensed under a Creative Commons Attribution-NonCommercial 3.0 Unported Licence.

expresses a higher charge storage contribution owing to its larger surface area. According to the measured discharge Δt from the CV profiles, the specific capacitance (C) was determined using eqn (1), and the corresponding C as a function of the various current densities is depicted in Fig. S4(c).† The estimated value of C at 1 A g^{-1} of current density was found to be 700 F g^{-1} for the ZIF8-4, which is higher compared to those of the ZIF8-3 (350 F g^{-1}), ZIF8-2 (146 F g^{-1}) and ZIF8-1 (118 F g^{-1}) nanocrystal electrodes, and the detailed performance at the various current densities are shown in Fig. S4(c).†

To further validate the electrochemical performance, the CV and GCD studies were performed using 1 M KOH aqueous electrolytes, and the detailed outcomes are illustrated in Fig. 5. As shown in Fig. 5(a)–(d), the CV plots under various scan rates range from 10 to 100 mV s^{-1} for the ZIF8-1, ZIF8-2, ZIF8-3 and ZIF8-4 nanocrystal electrodes, respectively. It is envisioned from the CV profiles that all as-prepared electrodes displayed a strong redox peak with an extended background current, demonstrating that the behavior of the as-prepared electrodes can be described mainly as pseudocapacitors.[44,46] Importantly, it clearly validates the presence of a faradaic reaction at the electrode–electrolyte interface. Based on the CV plots for all as-prepared electrodes, they showed a similar trend to the integrated area of the CV, and the current response increased as the scan rates increased. Additionally, they possess oxidation and reduction characteristics without any distortion and change in the position, therefore proving the reversible electrochemical nature.[47,48] As shown in Fig. 5(e), the comparative CV profiles of the ZIF8-1, ZIF8-2, ZIF8-3 and ZIF8-4 nanocrystal electrodes were characterized in an applied potential window ranging from 0.1 to 0.6 V at a fixed scan rate of 10 mV s^{-1}, where the exfoliated ZIF8-4 nanocrystals yield the CV highest current response and maximum integral area. The results demonstrated that the ZIF8-4 nanocrystal electrode has more capacitance than other as-prepared electrodes because it is more electrochemically active. A GCD study was performed to probe the electrochemical performance in 1 M KOH aqueous electrolytes for the ZIF8-1, ZIF8-2, ZIF8-3 and ZIF8-4 nanocrystal electrolytes, and the corresponding results are portrayed in Fig. 5(f)–(i). Owing to the presence of a set of redox peaks, all the

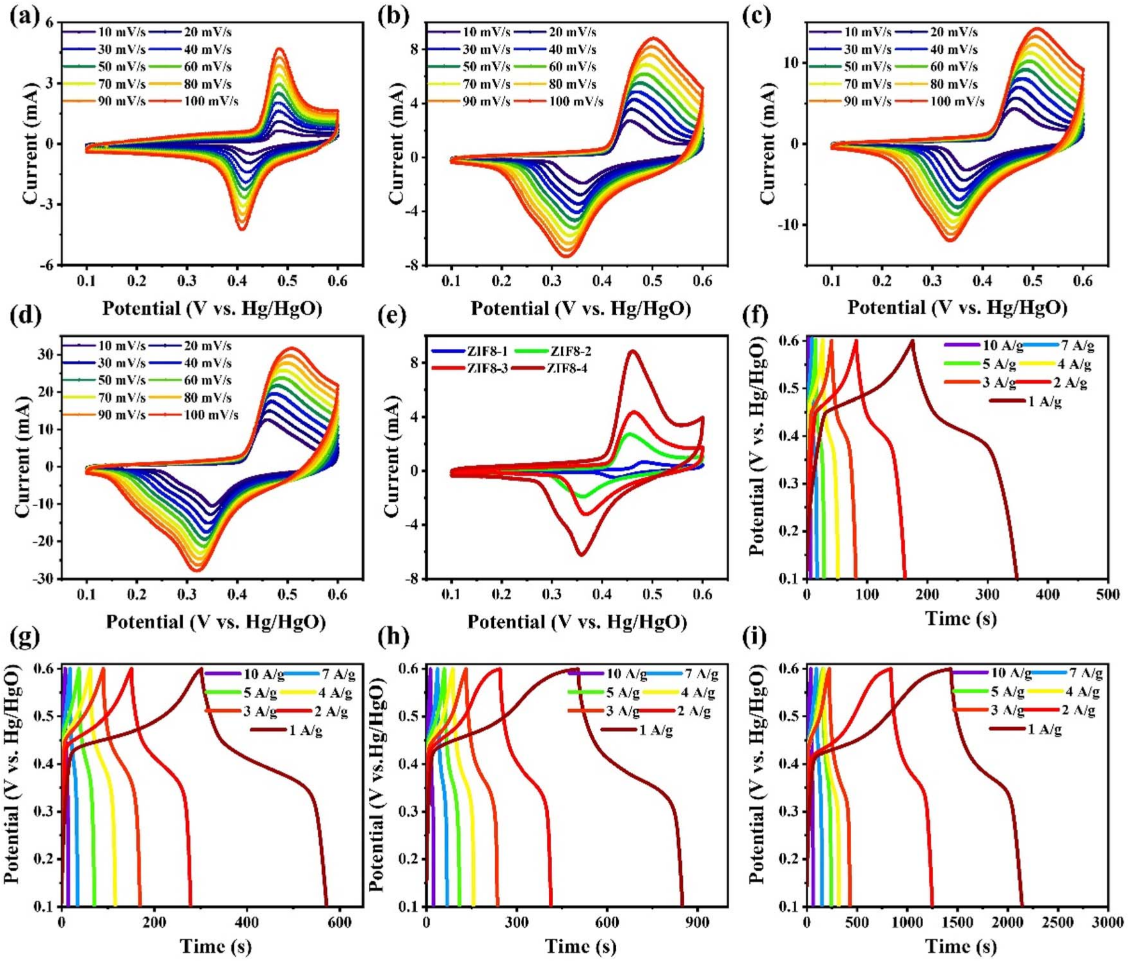

Fig. 5 Electrochemical performance of the series of ZIF8 nanocrystals in the three-electrode assembly: (a–d) cyclic voltammogram (CV) plots of the ZIF8-1, ZIF8-2, ZIF8-3 and ZIF8-4 nanocrystals under different sweep rates ranging 10–100 mV s^{-1}. (e) Comparative CV profiles for the ZIF8-1, ZIF8-2, ZIF8-3 and ZIF8-4 nanocrystals at an applied fixed sweep speed of 10 mV s^{-1} and (f–i) galvanostatic charging–discharging (GCD) profiles for the ZIF8-1, ZIF8-2, ZIF8-3 and ZIF8-4 nanocrystals under diverse current densities of 1, 2, 3, 4, 5, 7 and 10 A g^{-1}.

© 2024 The Author(s). Published by the Royal Society of Chemistry

Open Access Article. Published on 02 January 2024. Downloaded on 1/16/2026 5:07:56 PM.
This article is licensed under a Creative Commons Attribution-NonCommercial 3.0 Unported Licence.

as-prepared electrodes showed non-linear GCD plots, which confirms the pseudocapacitors, and the results are consistent with the CV results.

Moreover, the GCD profiles for the ZIF8-1, ZIF8-2, ZIF8-3 and ZIF8-4 nanocrystal electrodes were examined at a fixed current density of 0.5 A g^{-1}, and the results are depicted in Fig. 6(a). Compared with the ZIF8-1, ZIF8-2, and ZIF8-3 nanocrystal electrodes, the ZIF8-4 nanocrystal electrode showed a longer discharging period under a low current density, which can validate the highest charging capacity. The higher capacity of the ZIF8-4 nanocrystal electrode may be ascribed to the higher surface area and mesoporous morphology, which prominently afforded various channels for the fast diffusion and amenities of the electrolyte ions into the inside, thereby resulting in electrochemical performance. The assessed *C* values of the ZIF8-4 nanocrystal electrode were 1420, 1352, 1260, 1051.2, 980.7, 756, and 640 F g^{-1} at current densities of 1, 2, 3, 4, 5, 7 and 10 A g^{-1}, respectively. Meanwhile, detailed *C* performance was conducted for the other three electrodes, and their detailed results are presented in Fig. 6(b). Based on these calculations and observations, the ZIF8-4 nanocrystal electrode had approximately 4.1-, 2.6- and 2-fold higher results compared with ZIF8-1, ZIF8-2 and ZIF8-3 nanocrystal electrodes, respectively. The obtained consequences were higher compared with previously published reports (Table S2†). A significant improvement in the charge storage performance for the 1 M KOH electrolyte was perceived owing to the rapid anionic mobility and maximum conductivity of K^+ ions compared to the H^+. These results suggest that the prepared ZIF8-4 nanocrystal electrode had considerable charging–discharging efficiencies. The electrochemical benefits from the ZIF8-4 nanocrystal electrode, larger surface area and highly mesoporous ZIF8-4 nanocrystal electrode in the electrochemical reaction.

To further probe the electrochemical behaviour of the electrodes, electrochemical impedance spectroscopy (EIS) was utilized to examine the equivalent series resistance, as shown in Fig. S5.† Nyquist plots of the series of the ZIF8 nanocrystal electrodes (ZIF8-1, ZIF8-2, ZIF8-3 and ZIF8-4 electrodes) within a frequency ranging from 100 kHz to 0.01 Hz by employing an open-circuit voltage of 5 mV in 1 M KOH aqueous electrolyte. The internal resistance of the electrode (R_s) indicates the electrolyte resistance and contact resistance among the active electrode material and current collector, and active material internal resistance, which can be attained from the point of Nyquist plot's interception on the *X*-axis.[36] Similarly, the charge transfer resistance (R_{ct}) can be assessed from the arc diameter of the semicircle that occurred in the high-frequency region.[45] The R_s of the electrodes was identified, and the calculated values were 5.2, 4.2, 3.2 and 2.2 Ω for the ZIF8-1, ZIF8-2, ZIF8-3 and ZIF8-4 nanocrystal electrodes, respectively. The obtained R_{ct} values of the ZIF8-1, ZIF8-2, ZIF8-3 and ZIF8-4 nanocrystal electrodes are 8, 5.4, 3.2 and 1.22 Ω, respectively. Obviously, the determined R_s and R_{ct} values of the ZIF8-4 nanocrystal electrode are considerably lower compared with the other three designed ZIF8-1, ZIF8-2, and ZIF8-3 electrodes, which undoubtedly demonstrate excellent conducting properties and thus enhance redox electrochemistry.

3.3 Symmetric supercapacitor analysis (two-electrode set-up)

The symmetric supercapacitor (SSC) fabrication device of the as-synthesized materials is prepared by two identical pieces of electrodes using a wet separator, and the schematic illustration is presented in Fig. 7(a). The electrochemical behaviour of the ZIF8-4 nanocrystal SSC device was performed in a two-electrode set-up by employing the CV, GCD and EIS under ambient conditions, and the performance was compared with those of ZIF8-3 nanocrystal SSC devices. The applied potential window is an essential step in enhancing the energy density, and as the voltage window increases, the energy density is enhanced. The CV and GCD profiles were evaluated under different voltage windows of 0.3, 0.5, 0.8 and 1 V at 10 mV s^{-1} of scan rate and 10 A g^{-1} of current density, respectively, as depicted in Fig. 7(b) and (c). Notably, the CV and GCD plots did not contain any hydrogen or oxygen evolution peaks at a maximum potential of

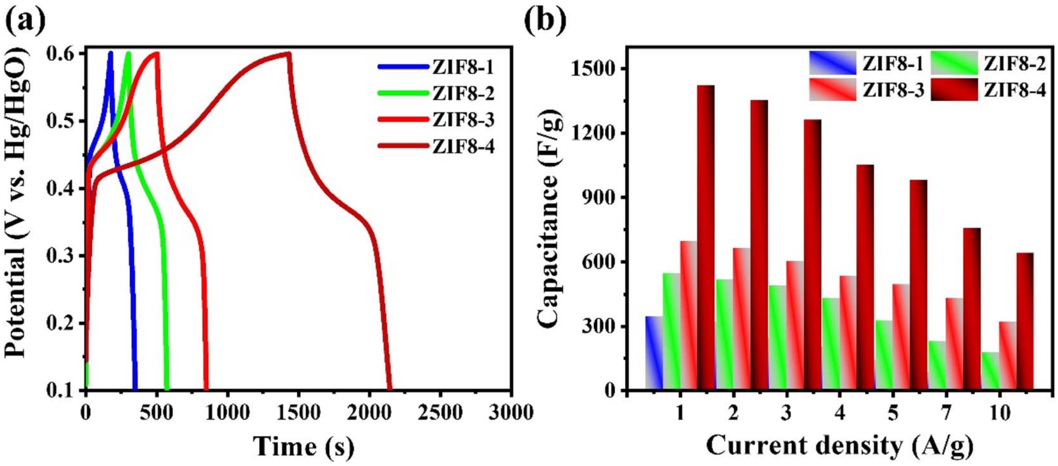

Fig. 6 Electrochemical performance of the series of ZIF8 nanocrystals in the three-electrode assembly: (a) comparative GCD profiles of the ZIF8-1, ZIF8-2, ZIF8-3 and ZIF8-4 nanocrystals at the applied fixed current density of 1 A g^{-1} and (b) a summary of the specific capacitance of the ZIF8-1, ZIF8-2, ZIF8-3 and ZIF8-4 nanocrystals as a function of different current densities.

Open Access Article. Published on 02 January 2024. Downloaded on 1/16/2026 5:07:56 PM.
This article is licensed under a Creative Commons Attribution-NonCommercial 3.0 Unported Licence.

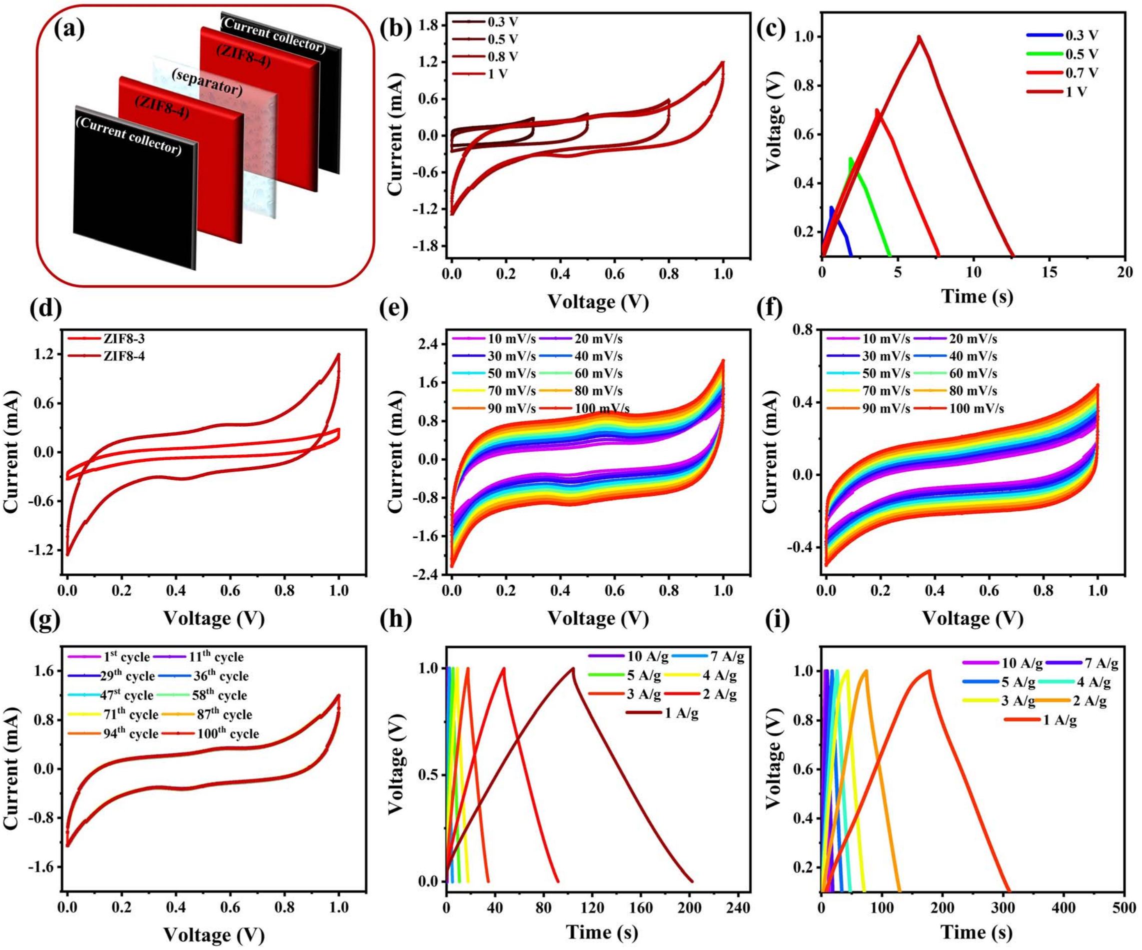

Fig. 7 Electrochemical performance of the optimized ZIF8-3 and ZIF8-4 nanocrystal SSCs in the two-electrode setup: (a) a schematic illustration of the symmetric supercapacitor device; (b and c) CV and GCD profiles at different applied voltages under 10 mV s^{-1} of scan rate and 10 A g^{-1} of current density, respectively; (d) comparative CV profiles of the ZIF8-3 and ZIF8-4 nanocrystals at an applied fixed sweep speed of 10 mV s^{-1}; (e and f) CV plots of the ZIF8-3 and ZIF8-4 nanocrystals under different sweep rates ranging from 10–100 mV s^{-1}; (g) CV profiles of the ZIF8-4 nanocrystals at an applied fixed sweep speed of 10 mV s^{-1} over 100 cycles and (h and i) GCD profiles of the ZIF8-3 and ZIF8-4 nanocrystals under diverse current densities of 1, 2, 3, 4, 5, 7 and 10 A g^{-1}.

1 V, indicating that they possessed stable energy features. In this study, the maximum voltage window was fixed at about 1 V for the aforementioned reason. Fig. 7(d) depicts the compared CV profiles at 10 mV s^{-1} of scan rate in the voltage ranging from 0 to 1 V for the ZIF8-3 and ZIF8-4 nanocrystal SSC device. As expected, the larger integral area of CV profiles for the ZIF8-4 SSC device compared with the ZIF8-3 SSC device indicates that the ZIF8-4 SSC device shows the highest specific capacitance because of its high conductivity and larger surface area.

To further validate the electrochemical performance of the ZIF8-4 SSC device, CV scan rates ranging from 10 mV s^{-1} to 100 mV s^{-1} tests are performed. The CV profile of the ZIF8-4 SSC device exhibited symmetrical behaviour with a small hemp (set of redox peaks) during charging and discharging, suggesting both pseudocapacitance and EDLC behaviours in the ZIF8-4 SSC device, as shown in Fig. 7(e). In contrast, the ZIF8-3 SSC device CV profiles display symmetrical and rectangular shapes, demonstrating typical EDLC behaviour (Fig. 7(f)). All the CV shapes for the ZIF8-3 and ZIF8-4 SSC devices did not alter after increasing the scan rates from 10 to 100 mV s^{-1}, indicating a high capability rate.

To investigate the long-term stability of the optimized ZIF8-4 SSC device, the 100 consecutive CV cycles were performed at a scan rate of 10 mV s^{-1}. As depicted in Fig. 7(g), the conducted CV profile at every cycle was constant, confirming that the ZIF8-4 SSC device was stable. The GCD profiles of optimized ZIF8-3 and ZIF8-4 SSC devices at various current densities of 1, 2, 3, 4, 5, 7, and 10 A g^{-1} were further evaluated to probe the electrochemical behaviour within the voltage range of 0–1 V, as shown in Fig. 7(h) and (i). Ideal straight and symmetrical GCD curves for ZIF8-3 SSCs in response to non-redox reactions at the surface of the electrode–electrolyte (Fig. 7(h)). When the ZIF8-4 device was employed in SSCs, the discharging plots were nonlinear at a low current density because of the high penetration of electrolyte ions; the results are presented in Fig. 7(i). It is well-known that the faradaic reaction is expedited at a high current density, which reduces the diffusion of the electrolyte ions to the active sites and improves the formation of the

Open Access Article. Published on 02 January 2024. Downloaded on 1/16/2026 5:07:56 PM.
This article is licensed under a Creative Commons Attribution-NonCommercial 3.0 Unported Licence.

electrostatic charge layer, thereby dropping the total capacitance. To further evaluate the electrochemical performance, EIS performed from 100 kHz to 0.01 Hz at the open circuit voltage is employed in Fig. S6.† The R_s of ZIF8-3 and ZIF8-4 SSC devices are found to be 8.37 and 7 Ω, respectively. The Nyquist plots in the low-frequency region of the ZIF8-4 SSC device show a more vertical shape, revealing better capacitance behavior. The semicircle diameter of the ZIF8-4 SSC device is the smallest compared to the ZIF8-3 SSC device (5.6 Ω), indicating the lowest R_{ct}, which is 2.4 Ω at the high-frequency region. The ZIF8-4 SSC device exhibits excellent electrochemical performance.

The ZIF8-4 SSC device exhibits the longest discharging, which is two-fold higher than that of the ZIF8-3 SSC devices. The performance is consistent with the CV outcomes, and the consequences are shown in Fig. 8(a). The C values of the SSC devices were assessed from the discharge curves by employing eqn (2), and the results are depicted in Fig. 8(b). The C of the ZIF8-4 SSC device is 384 F g^{-1} at 1 A g^{-1} of current density, which is two-fold higher than that of the ZIF8-3 SSC device (196 F g^{-1}). The corresponding C values of the ZIF8-4 SSC device are found to be 350, 288, 258, 208, 180, 140 and 100 F g^{-1} and 196, 168, 108, 75.2, 56, 39.2 and 20 F g^{-1} for the ZIF8-3 SSC device at current densities 1, 2, 3, 4, 5, 7 and 10 A g^{-1}, respectively. The possible reason for the higher C of the ZIF8-4 SSC device is because of its high electronic conductivity and larger surface area. The detailed obtained results are shown in Fig. 8(b) for all the SSC devices as a function of various current densities.

From a practical viewpoint, the cycling stability of a symmetric device is another important factor. The cyclic stability of the ZIF8-3 and ZIF8-4 SSC devices was further determined from the GCD profile at a current density of 10 A g^{-1} using 7000 cycles, and the results are shown in Fig. 8(c). The C of the ZIF8-4 SSC device was 100% when the symmetric device was employed until 3000 cycles. Then, 3%, 5%, 8% and 10% losses were observed after employing the 4000, 5000, 6000 and 7000 cycles, respectively, indicating that the device is highly stable because of the good conductivity compared with the ZIF8-3 SSC device (86% over 7000 cycles).

Energy density (E) and power density (P) were further determined using eqn (3) and (4) compared to the Ragone plot, as displayed in Fig. 8(d). The ZIF8-4 SSC device exhibited a maximum energy density of 43.7 W h kg^{-1} at a power density of 900 W kg^{-1} when the current density was 1 A g^{-1}, which is two-fold higher than that of the ZIF8-4 SSC device (24.5 W h kg^{-1} at 900 W kg^{-1}), suggesting an even higher performance of energy and power density compared to the previously published literature, as detailed studies are illustrated in Table 2.

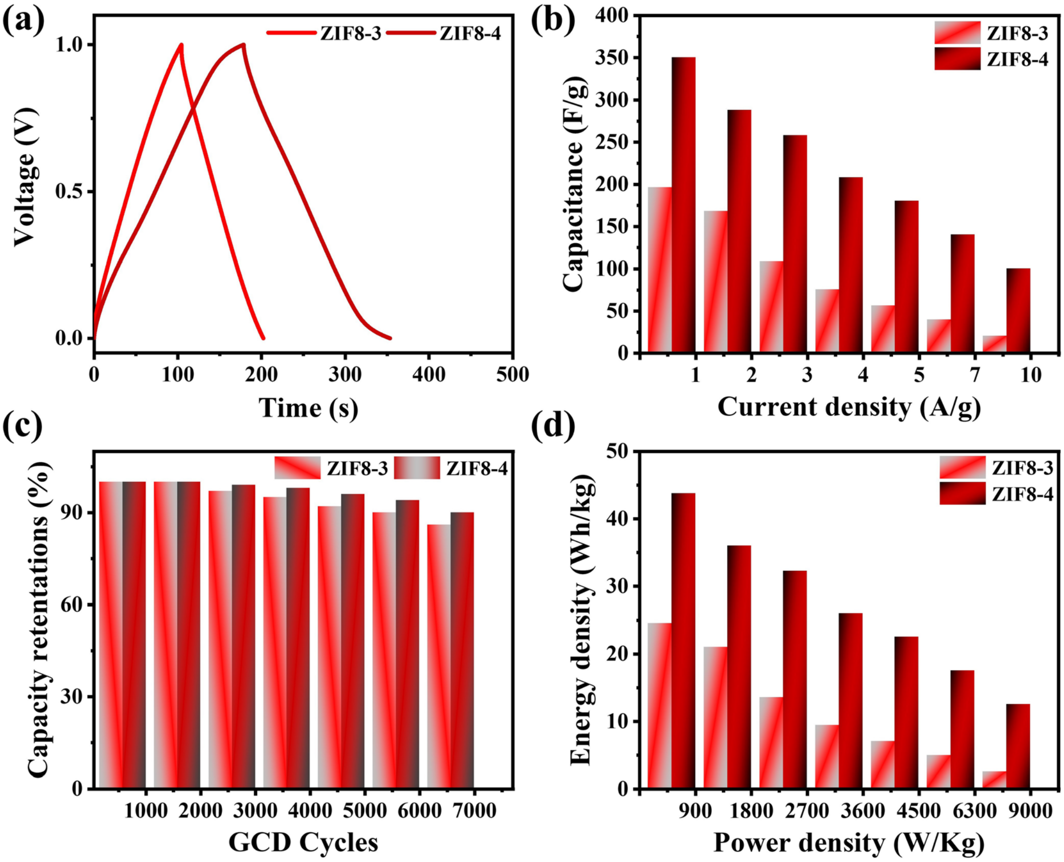

Fig. 8 Electrochemical performance of the optimized ZIF8-3 and ZIF8-4 nanocrystal SSCs in the two-electrode setup; (a) comparative GCD profile at 1 A g^{-1} of current density, (b) C values as a function of different current densities, (c) cycling stability using GCD profile over 7000 cycles and (d) Ragone plot.

Open Access Article. Published on 02 January 2024. Downloaded on 1/16/2026 5:07:56 PM.
This article is licensed under a Creative Commons Attribution-NonCommercial 3.0 Unported Licence.

Table 2 Comparable electrochemical performance of various ZIFs and TMO based materials in a two-electrode system

Electrode material	Electrolyte	C_s (F g^{-1})/current density (A g^{-1})	Power density (W kg^{-1})	Energy density (W h kg^{-1})	Cyclic stability (%)	Ref.
ZIF8-4 SSCs	**1 M KOH**	**350/1**	**900**	**43.7**	**90/7000**	**This work**
ZIF8-3 SSCs	**1 M KOH**	**196/1**	**900**	**24.5**	**86/7000**	
ZIF-67@NPC-800	0.5 M H_2SO_4	62/2	700	19.6	—	49
ZADV@LSC	—	250@0.8	586	19.7	89/5000	
ZIF-67@hetero-fNCs	Na_2SO_4 gel	77.9/0.5	1440	30	89.5/5000	50
ZIF-67@M-Co_3O_4	2 M KOH	134/1	790.7	46.5	86.4/8000	51
ZIF-67@v-CO_3O_4/CC	PVA/LiOH	145/1.3	915	45.3	84.1/5000	52
ZIF-67@Co_3O_4–CeO_2	3 M KOH	139.9/1	849.9	54.9	98/6000	53
ZIF-67@3D hollow $CoWO_4$	2 M KOH	81/0.5	404	29	—	54
$NiCo_2O_4$/MnO_2//biochar	6 M KOH	85/1	133.5	30.4	85/5000	55
$NiCo_2O_4$/CoFe LDH//AC	2 M KOH	64.7/1	950	28.9	76.9/5000	56
$2Fe_2O_3$/RGO/Fe_3O_4	2 M KOH	6.9/20	661.5	4.1/	97/2000	57
MO:ZnO@NF//AC	3 M KOH	125.2/1	778	39	75.6/8000	58
Nb/Co-NDPC	1 M KOH	293/0.5	—	—	82/15 000	59

4. Conclusion

In summary, we demonstrated a series of ZIF8 nanocrystals systematically through a cost-effective strategy under diverse synthesis conditions. The larger size was tuned into nano by varying the synthesis conditions, resulting in a larger surface area of ZIF8-4 (2800 m^2 g^{-1}). Owing to their larger surface area with uniform hexagonal morphology, the resultant ZIF8-4 nanocrystals were able to facilitate the larger active channels for quick diffusion and enable electrolyte ion into the inside of the electrode, therefore improving their SC performance. The SC studies were explored using different aqueous electrolytes (0.5 M H_2SO_4 and 1 M KOH) in the three-electrode set-up. The SC performance obtained using the basic electrolyte (1 M KOH) was higher owing to the higher ionic mobility of K^+. Significantly, the ZIF8-4 nanocrystal electrode showed a pseudocapacitance contribution with a maximum capacitance of 1420 F g^{-1} compared with ZIF8-1 (344.3 F g^{-1}), ZIF8-2 (545 F g^{-1}) and ZIF8-3 (693 F g^{-1}) at a current density of 1 A g^{-1} in three-electrode assembly. In addition, the fabricated SSC device employing the optimized ZIF8-4 offered 350 F g^{-1} with a maximum energy density of 43.7 W h kg^{-1} at a power density of 900 W kg^{-1} over 1 A g^{-1} of current density in a two-electrode setup. The practical implementations of the constructed ZIF8-4 SSC device were tested by performing 7000 GCD cycles at 10 A g^{-1}, and only 10% loss was noticed. These electrochemical findings demonstrate that the fabricated ZIF8-4 SSC device is promising from the viewpoint of applications in high-performance and extended lifetime energy-storage systems.

Conflicts of interest

There are no conflicts to declare.

Acknowledgements

This study was partly supported by the Korea Institute of Energy Technology Evaluation and Planning (KETEP; 20212050100010) and the Technology Innovation Program (20017464) funded by the Ministry of Trade, Industry & Energy (MOTIE, Korea).

References

1 P. Zhang, F. Sun, Z. Shen and D. Cao, ZIF-derived porous carbon: a promising supercapacitor electrode material, *J. Mater. Chem. A*, 2014, **2**(32), 12873–12880.

2 M. Manikandan, K. Subramani, M. Sathish and S. Dhanuskodi, Hydrothermal synthesis of cobalt telluride nanorods for a high performance hybrid asymmetric supercapacitor, *RSC Adv.*, 2020, **10**(23), 13632–13641.

3 D. Vikraman and et al, ., Engineering $MoTe_2$ and Janus SeMoTe nanosheet structures: first-principles roadmap and practical uses in hydrogen evolution reactions and symmetric supercapacitors, *Nano Energy*, 2021, **87**, 106161.

4 S. Hussain and et al, ., Hybrid design using carbon nanotubes decorated with Mo_2C and W_2C nanoparticles for supercapacitors and hydrogen evolution reactions, *ACS Sustain. Chem. Eng.*, 2020, **8**(32), 12248–12259.

5 M. Manikandan, D. K. Kulurumotlakatla, E. Manikandan, K. Karthigeyan and A. A. Al-Kahtani, Hydrothermal synthesis of rGO/ZnCoS composite for high performance asymmetric supercapacitor and HER applications, *J. Energy Storage*, 2023, **72**, 108769.

6 M. Manikandan, K. Subramani, S. Dhanuskodi and M. Sathish, One-pot hydrothermal synthesis of nickel cobalt telluride nanorods for hybrid energy storage systems, *Energy Fuels*, 2021, **35**(15), 12527–12537.

7 S. Chen, M. Xue, Y. Li, Y. Pan, L. Zhu and S. Qiu, Rational design and synthesis of $Ni_xCo_{3-x}O_4$ nanoparticles derived from multivariate MOF-74 for supercapacitors, *J. Mater. Chem. A*, 2015, **3**(40), 20145–20152.

8 Y. Pan and et al, ., Cation exchanged MOF-derived nitrogen-doped porous carbons for CO_2 capture and supercapacitor electrode materials, *J. Mater. Chem. A*, 2017, **5**(20), 9544–9552.

© 2024 The Author(s). Published by the Royal Society of Chemistry

Open Access Article. Published on 02 January 2024. Downloaded on 1/16/2026 5:07:56 PM.
This article is licensed under a Creative Commons Attribution-NonCommercial 3.0 Unported Licence.

9 J. Xu, F. Xu, M. Qian, F. Xu, Z. Hong and F. Huang, Conductive carbon nitride for excellent energy storage, *Adv. Mater.*, 2017, **29**(31), 1701674.

10 M. Salanne and et al, ., Efficient storage mechanisms for building better supercapacitors, *Nat. Energy*, 2016, **1**(6), 1–10.

11 C. Bathula and et al, ., Highly efficient solid-state synthesis of Co_3O_4 on multiwalled carbon nanotubes for supercapacitors, *J. Alloys Compd.*, 2021, **887**, 161307.

12 L. Liu, Z. Niu and J. Chen, Unconventional supercapacitors from nanocarbon-based electrode materials to device configurations, *Chem. Soc. Rev.*, 2016, **45**(15), 4340–4363.

13 Z. Xiang and D. Cao, Porous covalent–organic materials: synthesis, clean energy application and design, *J. Mater. Chem. A*, 2013, **1**(8), 2691–2718.

14 G. Zhong, D. Liu and J. Zhang, The application of ZIF-67 and its derivatives: adsorption, separation, electrochemistry and catalysts, *J. Mater. Chem. A*, 2018, **6**(5), 1887–1899.

15 S. Wang and X. Wang, Multifunctional metal–organic frameworks for photocatalysis, *Small*, 2015, **11**(26), 3097–3112.

16 S. Wang, W. Yao, J. Lin, Z. Ding and X. Wang, Cobalt imidazolate metal–organic frameworks photosplit CO_2 under mild reaction conditions, *Angew. Chem., Int. Ed.*, 2014, **53**(4), 1034–1038.

17 C.-C. Wang, Y.-Q. Zhang, T. Zhu, P. Wang and S.-J. Gao, Photocatalytic degradation of methylene blue and methyl orange in a Zn (II)-based metal–organic framework, *Desalin. Water Treat.*, 2016, **57**(38), 17844–17851.

18 C.-D. Wu, A. Hu, L. Zhang and W. Lin, A homochiral porous metal–organic framework for highly enantioselective heterogeneous asymmetric catalysis, *J. Am. Chem. Soc.*, 2005, **127**(25), 8940–8941.

19 A. Corma, H. Garcia and F. Llabrés i Xamena, Engineering metal organic frameworks for heterogeneous catalysis, *Chem. Rev.*, 2010, **110**(8), 4606–4655.

20 D. Farrusseng, S. Aguado and C. Pinel, Metal–organic frameworks: opportunities for catalysis, *Angew. Chem., Int. Ed.*, 2009, **48**(41), 7502–7513.

21 W. Chaikittisilp, K. Ariga and Y. Yamauchi, A new family of carbon materials: synthesis of MOF-derived nanoporous carbons and their promising applications, *J. Mater. Chem. A*, 2013, **1**(1), 14–19.

22 Y. Kou, Y. Xu, Z. Guo and D. Jiang, Supercapacitive energy storage and electric power supply using an aza-fused π-conjugated microporous framework, *Angew. Chem.*, 2011, **123**(37), 8912–8916.

23 Q.-L. Zhu and Q. Xu, Metal–organic framework composites, *Chem. Soc. Rev.*, 2014, **43**(16), 5468–5512.

24 I. Rabani and et al, ., Structural engineering of ruthenium decorated zeolitic imidazole framework nanocomposite for hydrogen evolution reactions and supercapacitors, *J. Energy Storage*, 2023, **62**, 106885.

25 J. Gascon, M. D. Hernández-Alonso, A. R. Almeida, G. P. van Klink, F. Kapteijn and G. Mul, Isoreticular MOFs as efficient photocatalysts with tunable band gap: an operando FTIR study of the photoinduced oxidation of propylene, *ChemSusChem*, 2008, **1**(12), 981–983.

26 S. Gautam and et al, ., Metal oxides and metal organic frameworks for the photocatalytic degradation: a review, *J. Environ. Chem. Eng.*, 2020, **8**(3), 103726.

27 Y. Song, X. Li, L. Sun and L. Wang, Metal/metal oxide nanostructures derived from metal–organic frameworks, *RSC Adv.*, 2015, **5**(10), 7267–7279.

28 M. He, J. Yao, Q. Liu, Z. Zhong and H. Wang, Toluene-assisted synthesis of RHO-type zeolitic imidazolate frameworks: synthesis and formation mechanism of ZIF-11 and ZIF-12, *Dalton Trans.*, 2013, **42**(47), 16608–16613.

29 L. Zhang and et al, ., Highly graphitized nitrogen-doped porous carbon nanopolyhedra derived from ZIF-8 nanocrystals as efficient electrocatalysts for oxygen reduction reactions, *Nanoscale*, 2014, **6**(12), 6590–6602.

30 X. Li and et al, ., Supercapacitor electrode materials with hierarchically structured pores from carbonization of MWCNTs and ZIF-8 composites, *Nanoscale*, 2017, **9**(6), 2178–2187.

31 G. Xu and et al, ., Porous nitrogen and phosphorus co-doped carbon nanofiber networks for high performance electrical double layer capacitors, *J. Mater. Chem. A*, 2015, **3**(46), 23268–23273.

32 M. Jiang, X. Cao, D. Zhu, Y. Duan and J. Zhang, Hierarchically porous N-doped carbon derived from ZIF-8 nanocomposites for electrochemical applications, *Electrochim. Acta*, 2016, **196**, 699–707.

33 V. Veerasamy and et al, ., Nitrogen doping of highly tetrahedral amorphous carbon, *Phys. Rev. B: Condens. Matter Mater. Phys.*, 1993, **48**(24), 17954.

34 I. Rabani, K. Karuppasamy, D. Vikraman, H.-S. Kim and Y.-S. Seo, Hierarchical structured nano-polyhedrons of CeO_2@ZIF-8 composite for high performance supercapacitor applications, *J. Alloys Compd.*, 2021, **875**, 160074.

35 S. Zhou, X. Kong, B. Zheng, F. Huo, M. Strømme and C. Xu, Cellulose nanofiber@conductive metal–organic frameworks for high-performance flexible supercapacitors, *ACS Nano*, 2019, **13**(8), 9578–9586.

36 I. Rabani, J. Yoo, C. Bathula, S. Hussain and Y.-S. Seo, The role of uniformly distributed ZnO nanoparticles on cellulose nanofibers in flexible solid state symmetric supercapacitors, *J. Mater. Chem. A*, 2021, **9**(19), 11580–11594.

37 K. Kida, M. Okita, K. Fujita, S. Tanaka and Y. Miyake, Formation of high crystalline ZIF-8 in an aqueous solution, *CrystEngComm*, 2013, **15**(9), 1794–1801.

38 A. Schejn and et al, ., Cu^{2+}-doped zeolitic imidazolate frameworks (ZIF-8): efficient and stable catalysts for cycloadditions and condensation reactions, *Catal. Sci. Technol.*, 2015, **5**(3), 1829–1839.

39 J. Li and et al, ., Synthesis and adsorption performance of La@ZIF-8 composite metal–organic frameworks, *RSC Adv.*, 2020, **10**(6), 3380–3390.

40 M. T. Thanh, T. V. Thien, P. D. Du, N. P. Hung and D. Q. Khieu, Iron doped zeolitic imidazolate framework

© 2024 The Author(s). Published by the Royal Society of Chemistry

Open Access Article. Published on 02 January 2024. Downloaded on 1/16/2026 5:07:56 PM.
This article is licensed under a Creative Commons Attribution-NonCommercial 3.0 Unported Licence.

(Fe-ZIF-8): synthesis and photocatalytic degradation of RDB dye in Fe-ZIF-8, *J. Porous Mater.*, 2018, **25**(3), 857–869.

41 G. Kumari, K. Jayaramulu, T. K. Maji and C. Narayana, Temperature induced structural transformations and gas adsorption in the zeolitic imidazolate framework ZIF-8: a Raman study, *J. Phys. Chem. A*, 2013, **117**(43), 11006–11012.

42 D. Radhakrishnan and C. Narayana, Guest dependent Brillouin and Raman scattering studies of zeolitic imidazolate framework-8 (ZIF-8) under external pressure, *J. Chem. Phys.*, 2016, **144**(13), 134704.

43 L. M. Markham, L. C. Mayne, B. S. Hudson and M. Z. Zgierski, Resonance Raman studies of imidazole, imidazolium, and their derivatives: the effect of deuterium substitution, *J. Phys. Chem.*, 1993, **97**(40), 10319–10325.

44 I. Rabani, Y.-J. Park, J.-W. Lee, M. S. Tahir, A. Kumar and Y.-S. Seo, Ultra-thin flexible paper of BNNT–CNF/ZnO ternary nanostructure for enhanced solid-state supercapacitor and piezoelectric response, *J. Mater. Chem. A*, 2022, **10**(29), 15580–15594.

45 I. Rabani and et al, ., 1D-$CoSe_2$ nanoarray: a designed structure for efficient hydrogen evolution and symmetric supercapacitor characteristics, *Dalton Trans.*, 2020, **49**(40), 14191–14200.

46 I. Rabani, J. Yoo, H.-S. Kim, S. Hussain, K. Karuppasamy and Y.-S. Seo, Highly dispersive Co_3O_4 nanoparticles incorporated into a cellulose nanofiber for a high-performance flexible supercapacitor, *Nanoscale*, 2021, **13**(1), 355–370.

47 I. Rabani, A. Younus, S. Patil and Y.-S. Seo, Fabrication of Fe_3O_4-incorporated MnO_2 nanoflowers as electrodes for enhanced asymmetric supercapacitor performance, *Dalton Trans.*, 2022, **51**(37), 14190–14200.

48 I. Rabani, R. Zafar, K. Subalakshmi, H.-S. Kim, C. Bathula and Y.-S. Seo, A facile mechanochemical preparation of Co_3O_4@g-C_3N_4 for application in supercapacitors and degradation of pollutants in water, *J. Hazard. Mater.*, 2021, **407**, 124360.

49 N. L. Torad and et al, ., Electric double-layer capacitors based on highly graphitized nanoporous carbons derived from ZIF-67, *Chem.–Eur. J.*, 2014, **20**(26), 7895–7900.

50 G. Zhao and et al, ., Flexible nitrogen-doped carbon heteroarchitecture derived from ZIF-8/ZIF-67 hybrid coating on cotton biomass waste with high supercapacitive properties, *Microporous Mesoporous Mater.*, 2020, **303**, 110257.

51 G. Wei, Z. Zhou, X. Zhao, W. Zhang and C. An, Ultrathin metal–organic framework nanosheet-derived ultrathin Co_3O_4 nanomeshes with robust oxygen-evolving performance and asymmetric supercapacitors, *ACS Appl. Mater. Interfaces*, 2018, **10**(28), 23721–23730.

52 X. Fan and et al, ., Asymmetric supercapacitors utilizing highly porous metal-organic framework derived Co_3O_4 nanosheets grown on Ni foam and polyaniline hydrogel derived N-doped nanocarbon electrode materials, *Chem. Phys. Lett.*, 2017, **689**, 162–168.

53 C. Wei and et al, ., Self-template synthesis of hybrid porous Co_3O_4–CeO_2 hollow polyhedrons for high-performance supercapacitors, *Chem.–Asian J.*, 2018, **13**(1), 111–117.

54 D. Chu and et al, ., 3D Hollow Flower-like $CoWO_4$ Derived from ZIF-67 Grown on Ni-foam for High-Performance Asymmetrical Supercapacitors, *Chem.–Asian J.*, 2020, **15**(11), 1750–1755.

55 B. Ren, M. Fan, X. Yang, L. Wang and H. Yu, 3D Hierarchical structure Electrodes of MnO_2 Nanosheets Decorated on Needle-like $NiCo_2O_4$ Nanocones on Ni Foam as a Cathode Material for Asymmetric Supercapacitors, *ChemistrySelect*, 2019, **4**(19), 5641–5650.

56 W. Chen and et al, ., Hierarchical $NiCo_2O_4$@Co-Fe LDH core-shell nanowire arrays for high-performance supercapacitor, *Appl. Surf. Sci.*, 2018, **451**, 280–288.

57 C. Zhao, X. Shao, Y. Zhang and X. Qian, Fe_2O_3/reduced graphene oxide/Fe_3O_4 composite *in situ* grown on Fe foil for high-performance supercapacitors, *ACS Appl. Mater. Interfaces*, 2016, **8**(44), 30133–30142.

58 A. Ali and et al, ., Mo-doped ZnO nanoflakes on Ni-foam for asymmetric supercapacitor applications, *RSC Adv.*, 2019, **9**(47), 27432–27438.

59 C. Yang and et al, ., Tailoring the supercapacitive behaviors of Co/Zn-ZIF derived nanoporous carbon *via* incorporating transition metal species: a hybrid experimental-computational exploration, *Chem. Eng. J.*, 2021, **419**, 129636.

© 2024 The Author(s). Published by the Royal Society of Chemistry